IOP Publishing Biomed. Mater. 18 (2023) 025025 https://doi.org/10.1088/1748-605X/acbd09

Biomedical Materials

OPEN ACCESS

RECEIVED
29 April 2022

REVISED
2 February 2023

ACCEPTED FOR PUBLICATION
17 February 2023

PUBLISHED
1 March 2023

PAPER

Cell-contact-mediated assembly of contractile airway smooth muscle rings

Jonathan Tjong[1], Stefan Pendlmayr[1], Jena Barter[1,2], Julie Chen[1], Geoffrey N Maksym[1,3], T Alexander Quinn[1,4] and John P Frampton[1,2,*]

[1] School of Biomedical Engineering, Dalhousie University, Halifax, Canada
[2] Department of Biochemistry & Molecular Biology, Dalhousie University, Halifax, Canada
[3] Department of Physics & Atmospheric Science, Dalhousie University, Halifax, Canada
[4] Department of Physiology & Biophysics, Dalhousie University, Halifax, Canada
[*] Author to whom any correspondence should be addressed.

E-mail: john.frampton@dal.ca

Keywords: tissue constructs, contractility, airway smooth muscle, soft tissue mechanics, transforming growth factor beta

Supplementary material for this article is available online

Abstract

Microtissues in the shape of toroidal rings provide an ideal geometry to better represent the structure and function of the airway smooth muscle present in the small airways, and to better understand diseases such as asthma. Here, polydimethylsiloxane devices consisting of a series of circular channels surrounding central mandrels are used to form microtissues in the shape of toroidal rings by way of the self-aggregation and -assembly of airway smooth muscle cell (ASMC) suspensions. Over time, the ASMCs present in the rings become spindle-shaped and axially align along the ring circumference. Ring strength and elastic modulus increase over 14 d in culture, without significant changes in ring size. Gene expression analysis indicates stable expression of mRNA for extracellular matrix-associated proteins, including collagen I and laminins α1 and α4 over 21 d in culture. Cells within the rings respond to TGF-β1 treatment, leading to dramatic decreases in ring circumference, with increases in mRNA and protein levels for extracellular matrix and contraction-associated markers. These data demonstrate the utility of ASMC rings as a platform for modeling diseases of the small airways such as asthma.

1. Introduction

Three-dimensional (3D) cell culture approaches, including the entrapment of cells in hydrogel matrices and the assembly of cells into compact aggregates such as spheroids, sheets, strips, and disks, have become instrumental to understanding cell–cell and cell-matrix interactions in the context of tissue development and are becoming increasingly important for evaluating novel therapeutics in the drug discovery pipeline [1–3]. Most strategies for 3D cell culture have focused on the development of relatively small (typically less than 200 μm-thick) monolithic structures to ensure efficient gas and nutrient exchange and to facilitate microscopic analysis [4, 5]. However, the development of 3D cell culture approaches for generating complex structures (e.g. tube-like structures) has become increasingly important for modeling blood vessels, lymphatic vessels, and other structures that conduct fluid [6], such as the airways. The tissue of the small airway is elastic and has an intrinsic stiffness that helps it to resist deformation when subject to the forces during breathing [7]. Advanced 3D cell culture systems for studying small airway physiology typically seek to organize co-cultured airway cells into layers, and often prioritize the ability to monitor contraction and force development in airway smooth muscle cells (ASMCs), as airway smooth muscle thickening, airway narrowing, and airway hyperresponsiveness (AHR) are key feature of small airway diseases such as asthma [8].

The approaches that exist for advanced 3D culture of airway cells vary considerably in complexity and capability, from relatively simple approaches (e.g. lung organoids and air–liquid interface (ALI) culture) to systems that require specialized fabrication strategies and instrumentation (e.g. lung-on-a-chip devices, microfabricated tissue gauges (μTUGs), and

bioprinted airway constructs). Lung organoid models typically use pluripotent stem cells that self-organize into structures that best reflect the organization of the developing lung [9, 10]. Lung organoids formed from a mixture of adult lung cell types also exhibit self-organization, but are limited in their ability to reliably form mature airway structures [11]. Air–liquid interface (ALI) cultures 'unfold' the airway wall by growing cells under static conditions on a semipermeable membrane with apical exposure to air, resulting in a well-differentiated epithelium with multiple epithelial cell types and distinct apical and basal surfaces [12, 13]. ALI cultures also facilitate co-culture with cells from the subepithelial layers, such as ASMCs [14]. Similar to ALI culture, lung-on-a-chip devices allow cells to grow on semipermeable membranes, but provide the option to expose cells to dynamic conditions such as fluid flow and cyclic stretch [15, 16]. These devices show promise in modeling vascular leakage in pulmonary edema and neutrophil recruitment in response to inflammation [16, 17]. Multi-chamber lung-on-a-chip devices have been used to co-culture epithelial cells with ASMCs to study cell–cell interactions involved in chronic obstructive pulmonary disease and asthma [18]. To monitor ASMC contractility, it is possible to culture ASMCs on flexible thin films that display differences in curvature upon contraction and relaxation of the ASMCs [19], or to assemble ASMC microtissues around μTUGs [20–23], which consist of arrays of pillars that deflect in the presence of tensile force. Finally, 3D bioprinting, where cells are deposited in a polymeric bio-ink into a desired structure, has been explored for modeling alveolar vasculature [24], epithelial-endothelial interactions in the small airway [25, 26], and for generating ASMC rings that respond to bronchoconstrictors, bronchodilators, and growth factors [27].

Although 3D cell culture offers some clear advantages over traditional 2D cell culture with respect to modeling the small airway, most approaches are limited in the ability to efficiently capture structure-function relationships in a format similar in geometry to the small airway [28–30]. Specifically, they fail in recapitulating the organization of ASMCs into helical bundles, as found between the outermost submucosa and the adventitia of the small airway [7, 31]. This structure-function relationship can be efficiently investigated by considering the tube-like structure of the small airway as a series of toroidal rings. Using relatively simple approaches whereby cells are deposited as suspensions into relief structures designed to limit the lateral dispersion of cells, it is possible to promote cell-contact-mediated assembly into complex microtissue shapes such as tori and honeycombs [32–34]. Uniquely, the resulting tori are non-homeomorphic with spheroids and introduce distinct mechanical stresses to the cells growing within the structure. To date, only vascular SMC structures have been generated using this approach, but a similar strategy may be particularly suitable for the culture of ASMCs, as their organization in bands around the airway submucosa may be physically approximated using self-supported tori [31, 33].

Here, we used customizable elastomeric devices to form airway microtissues in the shape of toroidal rings by taking advantage of the ability of ASMCs to self-assemble into contractile structures without the need for supplementation with exogenous extracellular matrix (ECM) proteins [32, 35]. We characterized the physical and biological properties of these tissue rings under various growth conditions over time. As ASMCs also demonstrate remarkable phenotypic plasticity, we examined ECM- and contractility-associated mRNA and protein levels following treatment with transforming growth factor beta 1 (TGF-β1), which is often elevated in the asthmatic airway, is known for its pro-fibrotic effect in other tissues, and is implicated in airway remodeling [36–38].

2. Materials and methods

2.1. Cell-contact-mediated assembly of ASMC rings

2.1.1. Device design and fabrication

To form rings from ASMC suspensions, an autoclavable polydimethylsiloxane (PDMS) device was developed. Key design iterations used throughout this work are presented in the cross-sectional line drawings in figure S1. The PDMS devices were cast from 3D-printed molds that were designed using Onshape software (Onshape). The molds were 3D printed using photopolymer resin and a B9Creator v1.2 3D printer (B9Creations). Post-processing of the resin mold was required prior to casting the PDMS devices [39]. The PDMS base and crosslinker (Sylgard 184, Dow Corning) were mixed in a 10:1 w/w ratio, placed under vacuum to remove trapped air bubbles, added to the post-processed resin mold, and then cured in a dry oven at 70 °C for at least 24 h.

2.1.2. Preparation of PDMS devices for cell culture

After removal from the 3D-printed molds, the PDMS devices were autoclave sterilized, then aseptically transferred into sterile 50 mm tissue culture plates. Surface treatment of the PDMS devices with the surfactant Pluronic F-127 was performed to limit cell adhesion to the PDMS [40]. Following treatment of the PDMS devices with 1% Pluronic F-127 solution for 24 h to sufficiently passivate the surface, the devices were rinsed with phosphate-buffered saline (PBS) twice, then pre-warmed to 37 °C. After the PBS was removed, the wells were seeded with freshly resuspended ASMCs.

2.1.3. ASMC culture

D12 (donor 12) Human ASMCs stably transfected with human telomerase reverse transcriptase (hTERT) were obtained from Dr William Gerthoffer (University of Nevada Reno). D12 ASMCs have been

previously characterized in both 2D and 3D cultures, and maintain the capacity for phenotype switching [21, 41]. The medium used for reviving the ASMCs from cryostorage consisted of 1:1 Dulbecco's Modified Eagle's Medium/Ham's F12 (DMEM/F12) base medium supplemented with 10% fetal bovine serum (FBS) and containing 1% penicillin–streptomycin–amphotericin B (Sigma). The medium used for routine ASMC maintenance and propagation, was the same except for a lower serum concentration (1% FBS). Cultures were maintained in a humidified cell culture incubator at 37 °C with 5% CO_2. Cells were harvested by trypsinization, pelleted, and resuspended in DMEM/F12 with 1% FBS. Unless otherwise noted, a total of 0.85×10^6 cells were added to each well of the PDMS device and allowed to settle undisturbed in the incubator for at least 1 h. Additional culture medium was then added to the larger chamber of the PDMS device. The rings were allowed to develop in standard cell culture conditions at 37 °C and 5% CO_2 for up to 21 d, with the culture medium refreshed every 48 h.

2.2. Airway microtissue mechanical analysis

2.2.1. Mechanical testing system

For uniaxial tensile testing, the rings were mounted between a programmable linear actuator (LM 1247-02-01, Faulhaber) and a load cell (PY2 72-4491, Harvard Apparatus) within a water-jacketed bath filled with PBS at a temperature of 37 °C using a recirculating water pump and heater [42]. The load cell was calibrated using known loads to give an output of 9.742 mN mV^{-1}, and it responded linearly over the strains applied to the rings during testing. A small baseline tare load was applied to remove slack within the tissue ring mounts, and ten cycles of preconditioning to approximately 10% strain were applied prior to the extension-to-failure tests. In the extension-to-failure tests, the tissue rings were pulled at a constant rate of 60 μm s^{-1} until rupture. Data were logged using LabChart (ADInstruments) and processed using custom Python code (Python 3.7) (see supplementary information).

2.2.2. Airway ring geometry measurements

For baseline tissue ring measurements, the tissue rings were fixed in 4% paraformaldehyde (PFA) immediately after removal from the mandrels since a gradual decrease in ring size occurred over time when live rings were free-floating. After fixation, the rings were moved to plates filled with PBS and allowed to settle to the bottom surface before imaging. Images were captured using a Nikon Eclipse Ti inverted microscope (Nikon Instruments). Measurements were performed using ImageJ by tracing the outer and inner ring circumferences. From the same images, the maximum and minimum widths along the rings were determined using custom Python code (see supplementary information).

2.2.3. Calculation of airway ring mechanical properties

Applied stress was calculated using the force measured from the load cell output distributed over twice the cross-sectional area of a ring. To obtain values for cross-sectional area, the rings were imaged at low magnification by bright field microscopy using a Nikon Eclipse Ti inverted microscope, and the widest and narrowest sections were used as the major and minor axes of an ellipse. For strain calculations, the linear actuator was calibrated and set to move at a constant rate of 60 μm s^{-1}. The unstrained initial length was determined from the average of the outer and inner ring circumference values divided by two.

2.3. Airway ring cell and gene expression analyses

2.3.1. Cell viability

Calcein-AM (C-AM; Biotium) was used to label live cells and propidium iodide (PI; Sigma-Aldrich) was used to label non-viable cells. Rings were stained with 3 μM C-AM for 30 min, then with 3 μM PI for 5 min, before being rinsed with PBS and imaged using a Nikon Eclipse Ti inverted microscope. ASMC rings were also assessed for metabolic activity as an index for viability using a CellTiter-Glo assay (Promega). Prior to performing the CellTiter-Glo assay, the ASMC rings were mechanically disrupted by repeated aspiration through a narrow pipette tip in the presence of the CellTiter-Glo cell lysis solution.

2.3.2. Cytoskeleton anisotropy

ASMC rings were fixed in 4% PFA for 20 min before quenching in 50 mM glycine in PBS and several rinses in PBS. Cells were permeabilized using Triton X-100 at 0.05% for 30 min at 4 °C and rinsed with PBS with 1% bovine serum albumin (BSA). Cells were stained for F-actin using TRITC-conjugated phalloidin (Millipore Sigma) at a concentration of 2 μg ml^{-1} in PBS with 1% BSA for 120 min before rinsing in PBS. Images of phalloidin-labeled actin were acquired using a LSM 710 confocal microscope (Zeiss). Alignment of F-actin was assessed with the Directionality Tool in Fiji (ImageJ) using nine bins between −90° and 90° to allow for 12.5° steps. Excluding the repeated ninth bin, the ratio of the size of the most-populated bin to the least-populated bin provided an index of the anisotropic alignment of cytoskeletal elements along a given direction.

2.3.3. Gene expression analysis

Total RNA was isolated from immortalized human D12 ASMCs using an Aurum Total RNA Mini Kit (Bio-Rad). The ASMC rings were lysed in the provided lysis buffer. Lysates were processed through an RNA-binding column and then treated with DNase to digest genomic DNA. The columns were thoroughly washed using the provided wash buffers, and the RNA sample was eluted using the provided elution buffer. A SPECTROstar Nano Microplate Reader with LVis Plate (BMG Labtech) was used to

determine total RNA concentrations in each sample at 260 nm. RNA quality was assessed using the ratio of absorbance at 260/280 nm. To obtain cDNA, first-strand cDNA synthesis of the total RNA was carried out using a qScript cDNA SuperMix single-step reaction mix (Quantabio, MA, USA). Target sequences were amplified using the primers listed in (table S1). Primers were selected for the product to span at least one exon-exon junction. Amplification was carried out using standard PCR with initial denaturation at 95 °C for 60 s, followed by 30 cycles of denaturation at 95 °C for 30 s, annealing at 50 °C for 30 s, and extension at 72 °C for 60 s, with a final extension at 72 °C for 300 s, using Taq Polymerase with ThermoPol Buffer and dNTP Solution Mix (New England BioLabs). Amplification products were separated on a 4% agarose gel, stained with SYBR Safe DNA Gel Stain (Invitrogen), and visualized using an Azure Biosystems c300 system (Azure Biosystems). Densitometric analysis was performed in ImageJ to calculate relative expression of each transcript and genes of interest were normalized to the geometric means of three housekeeping genes (GAPDH, RPLP0, and B2M) according to previously described methods [43].

2.3.4. Western blot analysis

ASMC ring lysates prepared in Laemmli sample buffer were loaded onto 4%–20% polyacrylamide gel electrophoresis (PAGE) gradient gels. Following PAGE, the proteins were transferred to 0.2 μM pore size polyvinylidene fluoride membranes. The membranes were then blocked for 1.5 h at room temperature in tris-buffered saline buffer containing 0.1% Tween 20 (TBST) and 5% BSA. Membranes were then incubated overnight at 4 °C in primary antibody solutions (see table S2 for details) containing 1% BSA in TBST. On the following day, the membranes were washed three times for 5 min per wash in TBST and incubated for 1 h at room temperature in secondary antibody solutions containing 1% BSA in TBST. The membranes were then washed three times for 5 min per wash in TBST. Finally, the membranes were incubated in SuperSignal West Pico (ThermoFisher) chemiluminescence substrate and images were recorded on an Azure C300 system (Azure Biosystems).

2.3.5. TGF-β1 treatment

ASMC rings were cultured in DMEM/F12 with 1% FBS for 7 d, with the medium refreshed every 48 h. At day 7, the medium was exchanged with fresh DMEM/F12 supplemented with insulin–transferrin–selenium (ITS) for 3 d prior to TGF-β1 exposure. The ASMC rings were then exposed to recombinant human TGF-β1 (ProSci) or vehicle and assessed after 3 d following removal of the rings from the PDMS device. After ∼1 min in PBS to allow the ASMC rings to contract, images were collected, and ring circumference values were calculated as described in section 2.2.2. Mechanical characterization was also conducted on TGF-β1-treated ASMC rings as described in section 2.1.

3. Results and discussion

Inspired by other strategies for microtissue assembly such as 3D aggregate culture, bioprinting, and micropatterned arrays [20, 44, 45], as well as previous devices utilizing agarose mandrels to promote the development of rings from vascular smooth muscle cells [33, 34, 46–49], a customizable PDMS device was developed and optimized for the fabrication of contractile rings from suspensions of ASMCs. Here, we found that the use of PDMS supported the production of reproducible and mechanically robust devices with relatively high aspect ratio features (figure S1). Through rapid prototyping and iterative design, a series of PDMS devices were developed to enable the efficient production of ASMC rings, and to facilitate ring maintenance and analysis (figures 1 and S1).

3.1. Cell-contact-mediated assembly of ASMC rings

ASMC rings were formed using a device featuring U-bottomed channels surrounding a conical mandrel. Figure 1(a) shows a 3D-printed mold from which a PDMS reverse replica can be cast (figure 1(b)) following a series of processing steps [39]. The PDMS device is designed to fit within a standard 50 mm culture dish (figure 1(c)), although this design can be modified to accommodate a range of cell culture formats including well-plates and larger culture dishes. Each device contains 6 mandrels, with each mandrel capable of forming an ASMC ring (figure 1(d)). The process for fabricating the ASMC rings using this device is simple and involves only a few steps (figure 1(e)). First, a suspension of ASMCs is dispensed into the circular channels surrounding the mandrels. The cells settle by gravity and partially assemble for several hours in a cell culture incubator before additional media is dispensed to fill the device. Finally, over the course of several days, the ASMC rings become progressively compact and begin to generate force. As the ASMC rings develop, the contractile force they generate causes them to move up the sloped lower section of the mandrel. A set of PDMS devices was also fabricated with flat-bottomed channels to better monitor ring development using light microscopy (figures 1(f)–(h) and S1(a)).

The ASMCs settled by gravity and began assembling into a contiguous layer in as little as 1 h (figure 1(f)). By two hours in culture, the layer of cells began to show signs of compaction around the central mandrel to form a ring-like structure. By 48 h, the process of ASMC ring formation was complete, and intact rings could be removed from the mandrels for analysis. The ease with which intact ASMC rings could be removed from the devices was influenced by the mandrel angle (defined as the angle

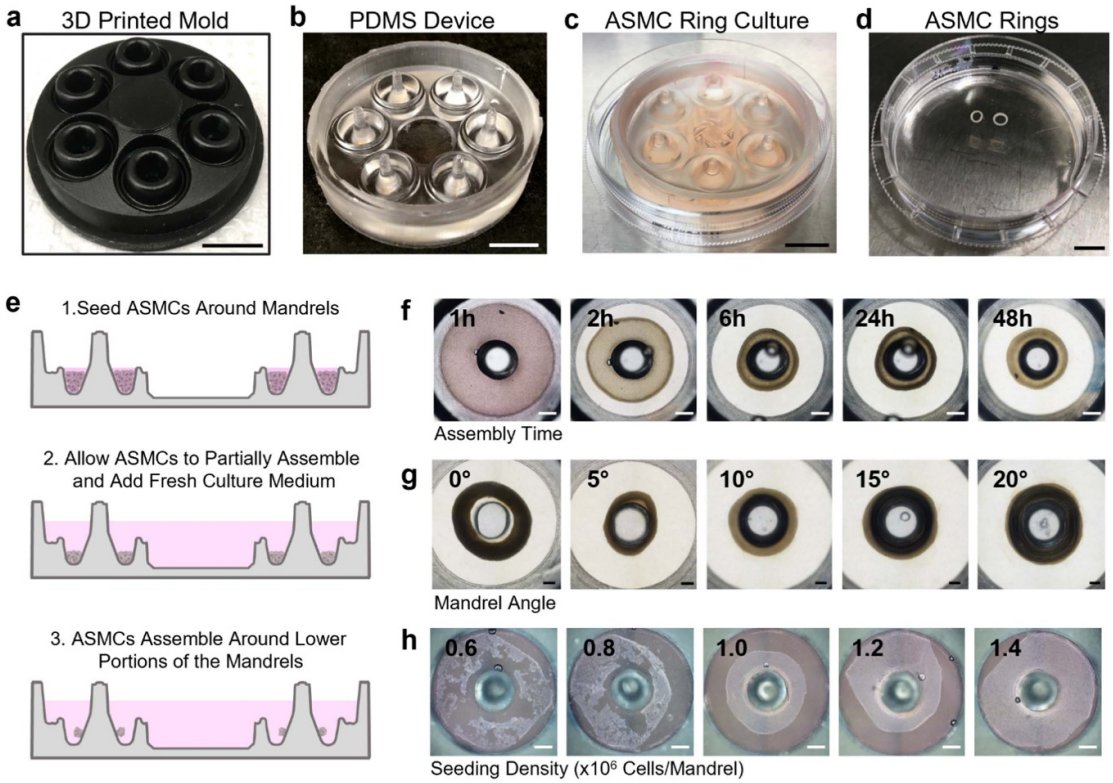

Figure 1. Cell-contact-mediated assembly of ASMC rings in PDMS cell culture devices. (a) Reusable 3D printed mold for casting PDMS devices. (b) As-cast PDMS reverse replica. (c) PDMS device prepared for cell culture placed within a standard 50 mm Petri dish. (d) Fully formed ASMC rings (day 7) after removal from the mandrels of the PDMS device. (e) Schematic representation of the process of cell seeding and ASMC development for the device with the geometry depicted in figure S1(b). (f) Ring development over time (circular channel width 2 mm; mandrel angle 10°; 1.0×10^6 cells/mandrel). (g) Ring development as a function of mandrel angle (circular channel width 2 mm; 1.0×10^6 cells/mandrel; 72 h in culture). (h) Ring integrity 2 h after cell seeding as a function of cell seeding density (circular channel width 2 mm; mandrel angle 10°). Scale bars in (a)–(d) are 10 mm. The images in (f)–(h) were captured using a device featuring flat-bottomed channels to facilitate microscopic visualization of the ring assembly process. Scale bars in (f)–(h) are 0.5 mm.

of the mandrel slope from the vertical axis). At low mandrel angles, parts of the ASMC rings were not in contact with the sides of the mandrels and remained at the bottom of the wells where they were difficult to access for removal from the devices (figure 1(g)). ASMC rings were most easily removed from devices with a mandrel angle of 20° after they moved up the sloped lower portion of the mandrel. Therefore, in the optimized device, the lower portion of the mandrel was designed to taper at an angle of 20° from vertical towards an upper section with a 2.4 mm diameter, whereas the upper portion of the mandrel was designed to taper at an angle of 3° from vertical towards a 2 mm diameter cap.

ASMC rings with cells connected along the entire circumference of the mandrel formed at cell seeding densities as low as 0.8×10^6 cells/mandrel (figure 1(h)). The provision of an environment where sufficient cell density allowed an evenly distributed, contiguous chain of cell–cell contacts was critical for the formation of intact rings. The final design iteration thus incorporated a U-bottomed channel to allow greater cell compaction after cell seeding (figure S1(a) and (b)). For these U-bottomed channels, a seeding density of 0.85×10^6 was optimal in terms of balancing the number of cells utilized for ASMC ring assembly with the success rate of ring formation, defined as the number of intact rings divided by the total number of rings attempted including rings that broke during development and those that failed to self-assemble (table S3).

3.2. ASMC rings remain viable for 21 d in culture

To assess cell viability within ASMC rings over time, live/dead staining was performed using C-AM and PI (figure 2(a)). At day 1 and day 3, a low percentage of non-viable cells of a similar proportion to those that die during routine cell passaging were dispersed throughout the mostly viable cells in the ASMC rings. These non-viable cells did not interfere with ring development and were in the same proportion as the number of non-viable cells present during routine 2D cell culture. After day 7, the relatively few non-viable cells that could be visualized by PI staining appeared to be localized in the core regions of the ASMC rings, while the intensely fluorescent C-AM labeled viable cells featured prominently throughout the ASMC rings. Closer inspection of C-AM-labeled ASMC rings revealed viable cells elongating with

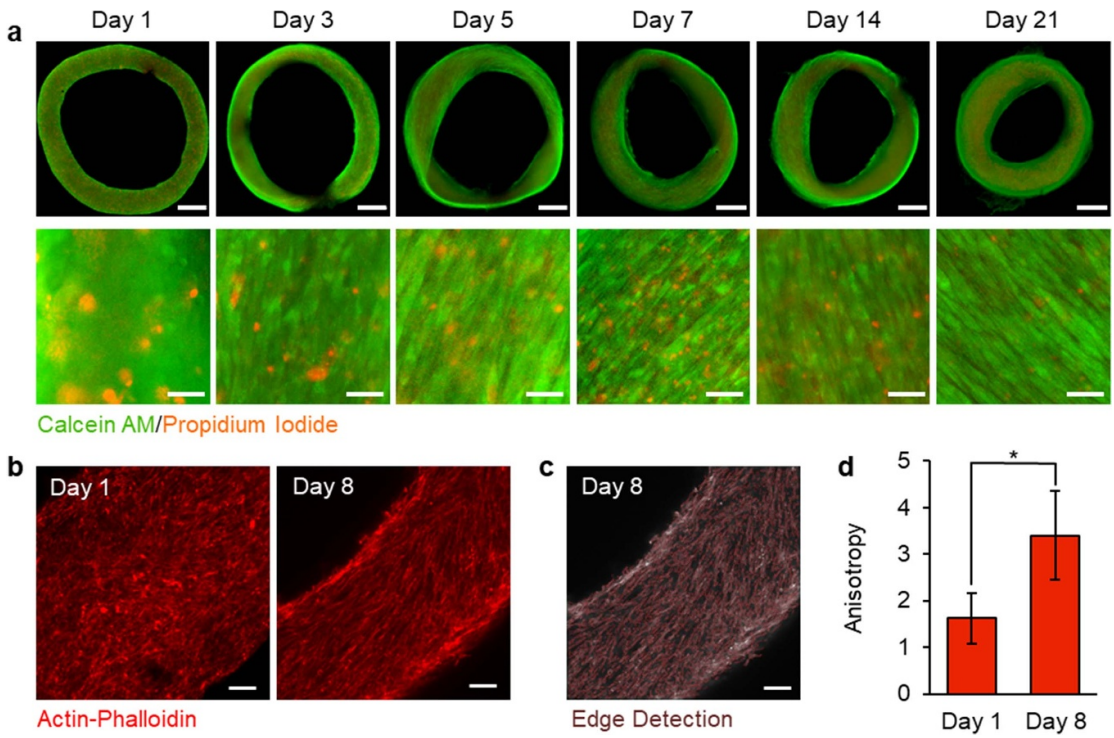

Figure 2. Viability and circumferential alignment of cells in ASMC rings after removal from the PDMS device. (a) The majority of ASMCs remain viable in rings over 21 d of culture. The top panel shows entire rings captured using a 2X magnification objective lens. The bottom panel shows images captured from a different set of rings using a 10X magnification objective lens with alignment of cells apparent from day 3 onwards. (b) Actin-phalloidin staining of ASMC rings demonstrates increased alignment of actin microfilaments with time in culture, as shown in single optical sections from confocal microscopy. (c) Feature extraction from an actin-phalloidin-stained sample by Canny edge detection. (d) Quantification of anisotropy at day 1 and day 8 of culture. Bars indicate mean values ± standard deviation, with $p < 0.05$ (denoted by *) considered statistically significant by Student's *t*-test. Scale bars in (a)–(c) are 50 μm.

respect to the circumference of the ASMC rings. Circumferential cell alignment was confirmed by confocal microscopy of actin-phalloidin-labeled ASMC rings (figure 2(b)). At day 1 of ASMC ring development, the actin filaments within the ASMCs were poorly aligned with respect to the ring circumference, whereas by day 8 of ASMC ring development the cells aligned their actin filaments approximately parallel to the ring circumference, which was visualized using Canny edge detection (ImageJ) to show cytoskeletal anisotropy (figures 2(c) and (d)).

To further quantify the viability of the cells in the ASMC rings, we measured the ATP content per ring using a CellTiter-Glo assay (figure S2). The measured ATP content per ring was highest at early time points (day 3; 9166 nM) and decreased over time (day 14; 3064 nM). There was no further decrease in metabolism between days 14 and 21, suggesting that by later time points in ASMC ring development, the cells entered a stable state. Because of the diffusion gradient intrinsic to 3D cell cultures, different zones within the tissue culture microenvironment can arise, with viable cells towards the surface, a quiescent intermediate zone, and non-viable cells within the core, especially as 3D tissues increase in size [50, 51]. The initial decrease in measured ATP may reflect the formation of these zones as cells transition from a 2D environment with even access to the supporting medium prior to seeding to 3D tissue aggregates after seeding in the PDMS device. In smaller ASMC constructs, such as in μTUGs, there are fewer cells between the interior of the construct and the supporting medium, so diffusion-limited regions are unlikely to form [21].

3.3. Serum concentration influences ASMC ring dimensions and mechanical properties

ASMCs display a marked degree of phenotypic plasticity, with the ability to take on opposing secretory/proliferative and contractile functions [52]. Since these changes to ASMC phenotype can be influenced by the presence of FBS [53], we examined the development of the ASMC rings at high and low concentrations of FBS (10% and 1%, respectively). Here, the ASMC rings were developed on the PDMS devices for over 14 d, allowing the channel and mandrel geometries to define the final ring dimensions. To assess the physical dimensions of intact ASMC rings during their development, rings in both high and low serum-supplemented media were removed from the mandrels and immediately fixed in PBS with 4% PFA at days 7 and 14. From these fixed ASMC rings, the outer circumference, inner circumference, minimum width, and maximum width values were recorded

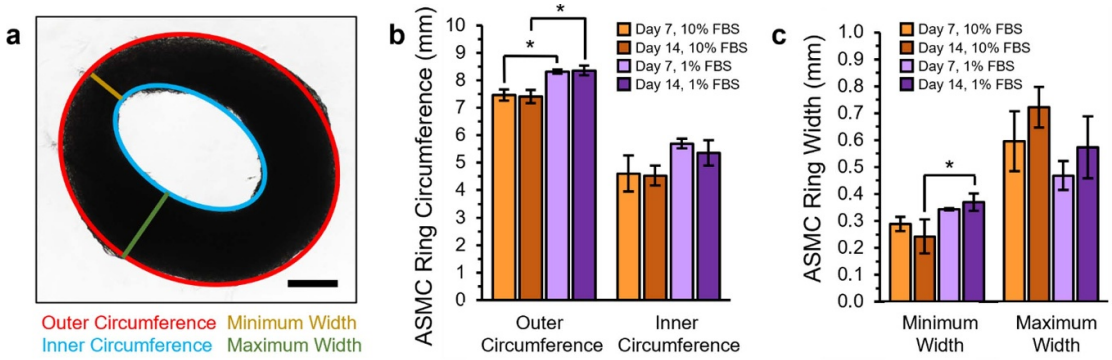

Figure 3. Ring geometry for different FBS concentrations. (a) Representative day 7 ASMC ring removed from the PDMS device following culture in medium containing 1% FBS. The outer circumference, inner circumference, minimum width, and maximum width are indicated by shaded lines. Scale bar is 250 μm. (b) Quantification of ASMC ring outer and inner circumference as a function of days in culture and FBS concentration. (c) Quantification of ASMC ring minimum and maximum width as a function of days in culture and FBS concentration. Bars in (b) and (c) indicate mean values ± standard deviation, with $p < 0.05$ (denoted by *) considered statistically significant by Tukey's multiple comparison test following one-way ANOVA.

(figure 3(a)). For all ASMC rings, the inner circumference (4926 ± 656 μm) was less than the minimum circumference of the central mandrel (6283 μm), suggesting the presence of intrinsic baseline tensile force within the ASMC rings that led to ring narrowing upon removal from the mandrels. ASMC rings cultured in medium containing 10% FBS had smaller outer circumference values compared to those cultured in medium containing 1% FBS at both day 7 and day 14 (figure 3(b)). This finding was unexpected, as the mitogenic effect of FBS might be expected to cause ring thickening [36]. Interestingly, ASMC rings grown in media supplemented with 10% FBS tended to develop non-uniformly about their circumference, in contrast to ASMC rings developed in media supplemented with 1% FBS, which were more uniform about their circumference. Analysis of minimum and maximum ASMC ring widths (figures 3(c) and S3) further demonstrated that ASMC ring geometry was more uniform across samples when the ASMC rings were cultured in medium supplemented with 1% versus 10% FBS.

To examine the mechanical properties of the ASMC rings, the rings were developed on the PDMS devices in 10% and 1% FBS-supplemented media and evaluated on days 7 and 14 by uniaxial tensile testing of live tissues mounted between a linear actuator and a force transducer (figure 4(a)). Preconditioning to approximately 10% strain over ten cycles produced the expected hysteresis between extension and relaxation during the initial cycles, which diminished with each preconditioning cycle (figure S4). Following preconditioning, the ASMC rings were extended at a constant rate of 60 μm s^{-1} until rupture. The force measured was normalized to twice the estimated cross-sectional area of the rings to obtain a stress–strain relationship (figure 4(b)). The peak stress at rupture was comparable at day 7 for ASMC rings developed in 10% versus 1% FBS (30.2 ± 6.7 vs. 34.4 ± 1.4 kPa, respectively), but by day 14 the peak stress of ASMC rings developed in 1% FBS was significantly greater than those developed in 10% FBS (52.5 ± 4.9 vs. 34.5 ± 8.1 kPa) (figure 4(c)). The peak strain at rupture was greater at day 7 and at day 14 for ASMC rings developed in 10% FBS compared to 1% FBS (1.41 ± 0.08 vs. 1.00 ± 0.10 at day 7 and 0.74 ± 0.12 vs. 1.04 ± 0.10 at day 14) (figure 4(d)). The tensile modulus values were comparable at day 7 and at day 14 between ASMC rings developed in 10% and 1% FBS (45.6 ± 9.9 vs. 39.9 ± 1.5 kPa at day 7 and 68.9 ± 5.5 vs. 71.0 ± 7.0 kPa at day 14), but a significant increase was noted between day 7 and day 14 for each of the FBS concentrations (figure 4(e)). Toughness, defined as the area below the stress–strain curve, was significantly greater at days 7 and 14 for ASMC rings developed in 1% FBS versus 10% FBS (18.6 ± 1.2 vs. 11.3 ± 3.4 μJ mm^{-3} at day 7 and 23.4 ± 3.8 vs. 9.8 ± 4.1 μJ mm^{-3} at day 14) (figure 4(f)). Compared to other engineered tissue rings, particularly those constructed from vascular SMCs, the ASMC tissue rings appeared to have a lower tensile modulus and peak stress (ultimate tensile stress/UTS), while also being more extensible [35, 46]. However, in general, the ASMC ring modulus values were comparable to those of excised ovine and porcine bronchial strips, as well as estimates of the human airway walls (although it should be noted that in many cases excised tissues include contributions from other tissue layers such as the airway submucosa and epithelium) [7, 54, 55].

3.4. TGF-β1 exposure leads to ASMC ring narrowing—a key feature of asthma

In asthma, the ASMCs in the small airways undergo significant changes termed airway remodeling that contribute to airway narrowing. Airway remodeling results in a noticeably thicker smooth muscle layer in sectioned asthmatic airways, with ASMC hypertrophy observed in the larger airways and hyperplasia observed in the smaller airways [56, 57]. In addition

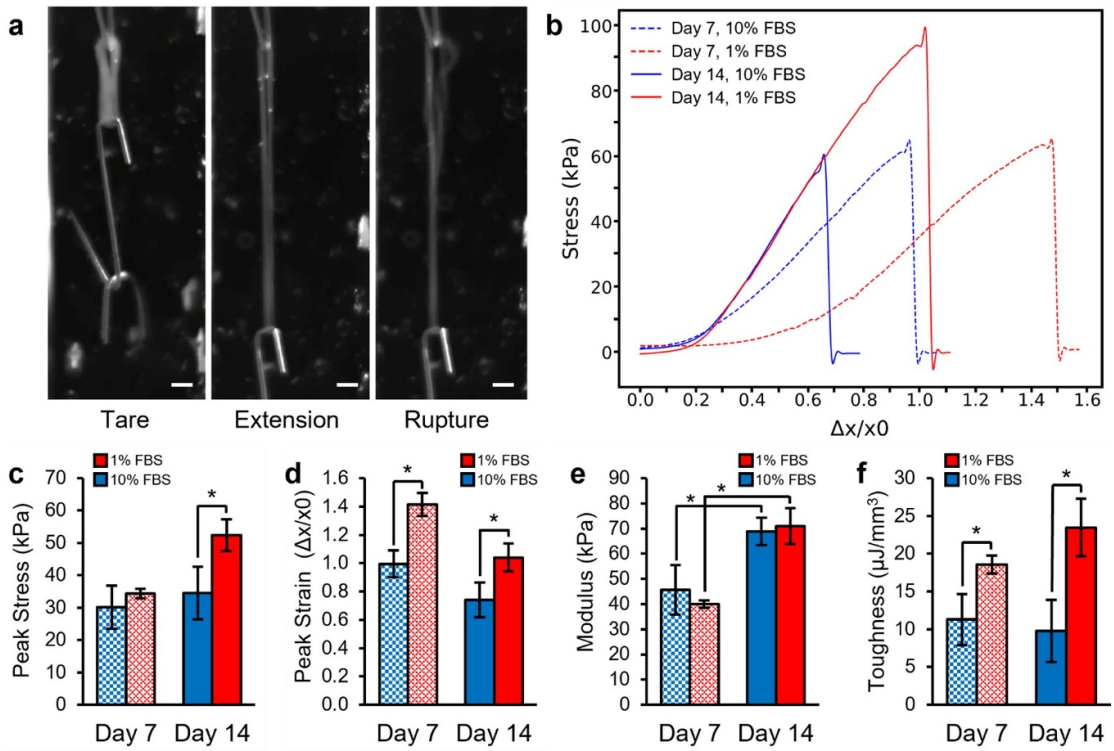

Figure 4. Mechanical properties of ASMC rings. (a) Setup for live ASMC ring mechanical testing showing a typical ASMC ring under no strain (tare), during extension, and following rupture. Scale bars are 1 mm. (b) Stress–strain curves for representative ASMC rings culture for either 7 d (dashed lines) or 14 d (solid lines) in either 10% FBS (blue) or 1% FBS (red). (c) Quantification of ASMC ring peak stress at rupture as a function of days in culture and FBS concentration. (d) Quantification of ASMC ring peak strain at rupture as a function of days in culture and FBS concentration. (e) Quantification of ASMC ring Young's modulus as a function of days in culture and FBS concentration. (f) Quantification of ASMC ring toughness as a function of days in culture and FBS concentration. Bars in (c)–(f) indicate mean values ± standard deviation for key comparisons discussed in the text, with $p < 0.05$ (denoted by *) considered statistically significant by Tukey's multiple comparison test following one-way ANOVA.

to narrowing the lumen, a thicker ASMC layer with greater cross-sectional area may be able to generate greater overall force, and alternatively, thicker ASMC may also have an impaired relaxation response to stretch, both of which can contribute to AHR [58, 59]. To evaluate the ASMC rings in terms of their suitability for modeling asthmatic airways, we exposed the rings to TGF-β1. TGF-β1 is one of several cytokines that are reported to be elevated in the airways of subjects with asthma, and its signaling can mediate some of the hallmark characteristics of asthmatic airways, including airway remodeling and AHR [60–63]. We compared the effect of introducing TGF-β1 to the ASMC rings at 1 and 10 ng ml^{-1} for three days following ASMC ring development in serum-free media. This was necessary as the effect of TGF-β1 on ASMCs can be highly context-dependent based on the presence of other growth factors which may be present in serum [64]. Images of the microtissues were captured at least 1 min after the rings were removed from the central mandrel. Rings that were given TGF-β1 at both 1 and 10 ng ml^{-1} were approximately 50% shorter along their inner circumference compared to control rings (2.81 ± 0.53 mm for 1 ng ml^{-1} TGF-β1 and 2.70 ± 0.55 mm for 10 ng ml^{-1} TGF-β1 vs. 5.13 ± 0.12) (figures 5(a) and (b)).

In other 3D tissue models composed of airway and vascular SMCs, the addition of TGF-β1 leads to changes in microtissue morphology accompanied by changes in the expression of ECM and contraction-associated proteins [27, 33]. For ASMCs and other smooth muscle cell types in 2D culture, TGF-β1 induces the expression of contractile phenotype markers, such as transgelin and α-smooth muscle actin (ACTA2/α-SMA), which likely contributes to cell shortening [65–67]. To investigate the role of TGF-β1 in altering the ASMC ring structure, we performed a semi-quantitative PCR analysis followed by a western blot analysis. TGF-β1 exposure can induce ASMC synthesis of ECM-associated proteins, which can contribute to airway remodeling, so we examined changes in the expression of ECM genes [68]. There was a significant increase in mRNA expression for collagen I (COL1A1) and fibronectin (FN1) with TGF-β1 exposure at both 1 and 10 ng ml^{-1}, but not for collagen III (COL3A1), laminin α2 (LAMA2), or laminin α4 (LAMA4) (figure 5(c)). We also examined the change in expression of markers associated with the smooth muscle contractile phenotype. There was a significant dose-dependent increase in the expression of mRNA for ACTA2 with TGF-β1 at both 1 and 10 ng ml^{-1} and an increase in the expression

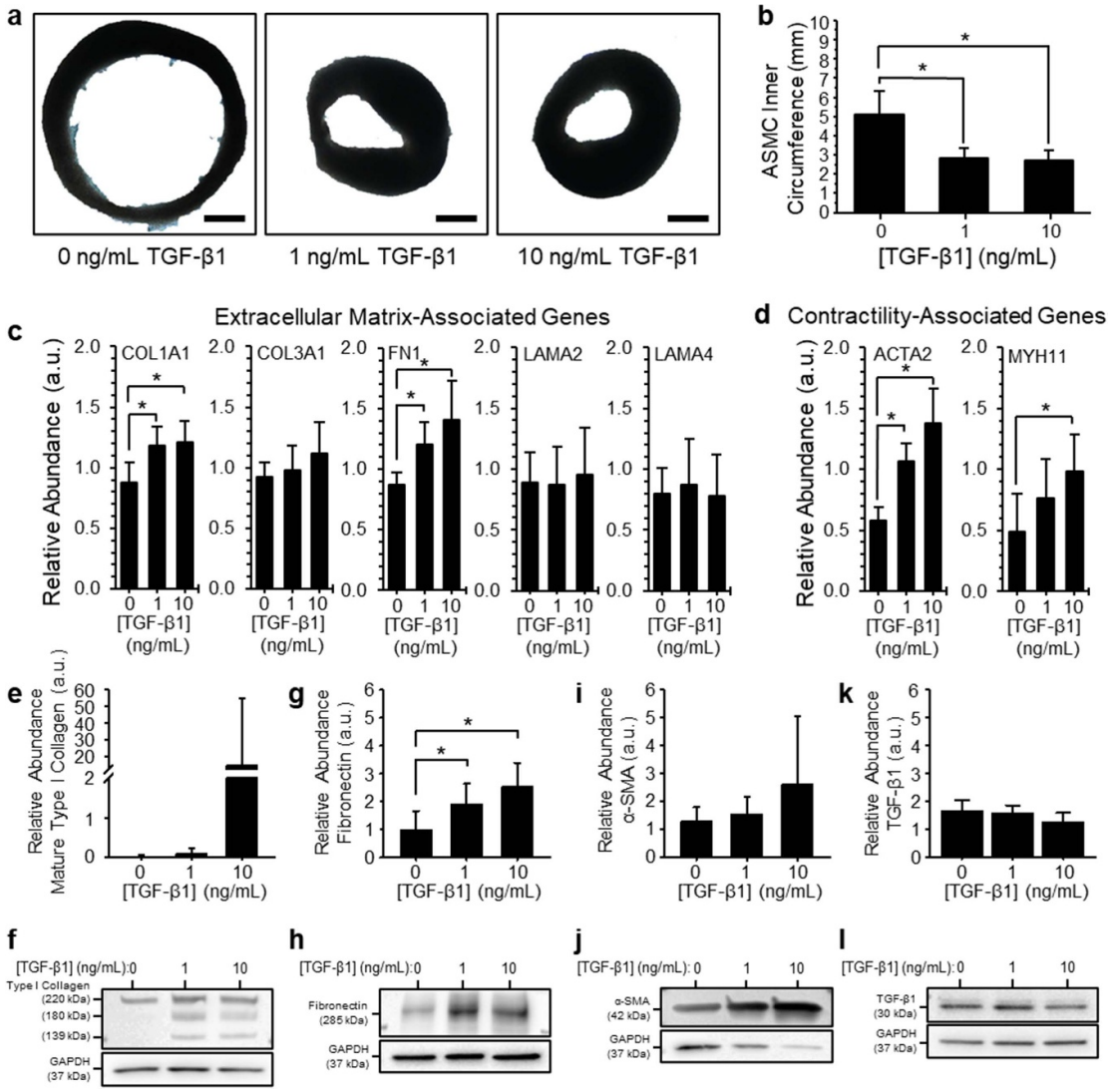

Figure 5. The contractile response of ASMC rings to TGF-β1. (a) Representative images of ASMC rings cultured in DMEM/F12 with ITS supplementation without TGF-β1 treatment and following treatment for 3 d in 1 ng ml^{-1} and 10 ng ml^{-1} TGF-β1 after removal from the PDMS device for 5 min. Scale bars are 500 μm. (b) Contraction of ASMC rings in response to TGF-β1 measured by way of ASMC ring circumference. (c) Expression of extracellular matrix-associated genes implicated in small airway disease remain relatively stable in response to TGF-β1, with significant dose-dependent increases in expression for COL1A1 and FN1. (d) Expression of contractility-associated genes implicated in small airway disease are elevated in response to TGF-β1. (e), (f) Levels of mature type I collagen protein (139 kDa band), as a function of TGF-β1 treatment. (g), (h) Levels of fibronectin protein, as a function of TGF-β1 treatment. (i), (j) Levels of α-SMA protein, as a function of TGF-β1 treatment. (k), (l) Levels of TGF-β1 protein produced by ASMC rings, as a function of applied TGF-β1 treatment. Bars in (b) indicate mean values $\pm$ standard deviation. Bars in (c) and (d) indicate geometric mean values $\pm$ standard deviation. Bars in (e), (k) indicate mean values $\pm$ standard deviation. For (b)–(d) and (e)–(k), $p < 0.05$ (denoted by *) was considered statistically significant by Tukey's multiple comparison test ((b)–(d)) or Student–Newman–Keuls multiple comparison test ((e)–(k)) following one-way ANOVA ($n \geqslant 3$ independent samples).

of mRNA for smooth muscle myosin heavy chain 11 (MYH11) after 10 ng ml^{-1} of TGF-β1 treatment (figure 5(d)). In 2D ASMC cultures, exposure to TGF-β1 leads to similar increases in the expression of ACTA2, FN1, and COL1A1 consistent with our tissue ring results [65, 66, 69]. There were no significant changes or trends toward differential expression of any of the ECM- and contractility-associated genes over 21 d in culture for rings that developed in the absence of TGF-β1 (figure S5).

To determine if changes in gene expression were reflected in corresponding protein levels in the ASMC rings, western blot analysis was performed for the ECM- and contractility-associated markers that were significantly elevated between non-TGF-β1-treated control samples and samples treated with both 1 and 10 ng ml^{-1} TGF-β1 (figures 5(e)–(j)). The levels of TGF-β1 produced by the ASMCs rings in response to the applied TGF-β1 treatment were also measured (figures 5(k) and (l)). Three bands were present for type I collagen, corresponding to pro-collagen (220 kDa), an intermediate precursor of mature collagen (180 kDa), and mature collagen (139 KDa). Across all samples and treatment conditions, the levels of mature type I collagen were low, with only one of the ASMC rings treated with 10 ng ml^{-1}

TGF-β1 producing appreciable quantities of mature type I collagen, as reflected in the large standard deviation for the 10 ng ml^{-1} TGF-β1 treatment in figure 5(e). As expected, based on previous studies of TGF-β1 treated ASMC cultures [66], levels of fibronectin increased significantly in response to TGF-β1 treatment. Levels of α-SMA and TGF-β1 produced by ASMCs did not increase significantly in response to applied TGF-β1 treatment, although a trend towards increased level of α-SMA with increasing concentration of applied TGF-β1 is evident in figure 5(i).

No changes in passive mechanical properties were noted following TGF-β1 treatment (figure S6), which is consistent with a lack of accumulation of collagen and elastin fibers. Therefore, the increase in ASMC ring contraction in response to applied TGF-β1 treatment observed here likely involve increased fibronectin and possibly α-SMA protein levels, which are suggested to be mediators of airway contractile response in small airway diseases [70, 71]. Levels of α-SMA and TGF-β1 produced by ASMCs did not increase significantly in response to applied TGF-β1 treatment, although a trend towards increased level of α-SMA with increasing concentration of applied TGF-β1 is evident in figure 5(i). No changes in passive mechanical properties were noted following TGF-β1 treatment (figure S6), which is consistent with a lack of accumulation of collagen and elastin fibers. Considering the known mitogenic and profibrotic effects of TGF-β1 on ASMCs, it was somewhat surprising that the application of TGF-β1 at either 1 or 10 ng ml^{-1} did not translate to changes in the passive mechanical properties of the rings. However, as demonstrated in figures 4(c)–(f), both time in culture and the presence of serum during ring formation altered the tissue mechanics, so the addition of TGF-β1 for only 3 d to growth-arrested ASMC rings may have been insufficient to elicit measurable changes. Furthermore, the composition of the ECM surrounding ASMCs in tissue rings has been shown previously to influence tissue mechanical properties [35]. It is possible that applying TGF-β1 for durations longer than 3 d or allowing the ASMC rings to further develop for additional time after TGF-β1 treatment could lead to measurable changes in the passive mechanical properties. In addition, increased stiffness of individual ASMCs treated with TGF-β1 can be observed by magnetic twisting cytometry, but may reflect changes to the cytoskeletal mechanics that contribute to active contractile processes rather than the overall mechanical properties of the construct [62]. Therefore, the increase in ASMC ring contraction in response to applied TGF-β1 treatment observed here can likely be attributed to increased fibronectin and possibly α-SMA protein levels, both of which are suggested to be mediators of airway contractile response in small airway diseases [70, 71].

TGF-β1 activates the Smad2/3 signaling pathway to modulate gene expression but can also act along alternate, non-Smad pathways that may additionally contribute to the changes observed in airway remodeling and AHR [65, 72–74]. Increased ACTA2 mRNA expression in response to TGF-β1 is likely mediated by RhoA/Rock activation (although it is interesting to note that TGF-β1 can also increase the translation of ACTA2 protein via PI3K) [66, 69]. The modest increase in MYH11 gene expression at only the higher concentration of TGF-β1 is consistent with observations that only a subpopulation of ASMCs in 2D culture demonstrate MYH11 expression [53, 69]. The ASMC ring model presented here represents a dramatically simplified signaling chain, without the contribution of other structural cells in the airways such as bronchial epithelial cells and fibroblasts (which are known to express, secrete, and respond to TGF-β1), as well as immune cells that participate in activation of TGF-β1 from its latent form through ECM remodeling [61, 63]. Nonetheless, elevated TGF-β1 may contribute to dysregulated signaling in asthmatic airways [75], and here we demonstrate using simplified engineered constructs, clear direct TGF-β1 effects of on ASMC rings, offering the potential to develop co-culture models to explore the contributions of these other cell types found in the small airways.

4. Conclusions and outlook

The overall objective of this work was to assess the feasibility and usefulness of ASMC tissue rings as a physiologically relevant *in vitro* cell culture model. We demonstrated that ASMC suspensions can be used to form ring-shaped microtissues without the need for exogenous ECM components or scaffold materials. The ASMC rings maintain viability over 21 d and display increased alignment of cytoskeletal structures as they develop. By characterizing their material properties, we also showed that the ASMC rings become stiffer over time. Using optimized cell culture conditions with 1% FBS, we were able to form robust rings, which were comparable to excised airways from animal models in terms of their material properties. Finally, with application of TGF-β1, a growth factor implicated in the pathology of asthma, there was a visible physical change in ASMC circumference, accompanied by shifts in mRNA expression profiles and protein levels.

By constraining cells in a ring-shaped channel, the ASMCs develop clear directionality and organization, better mimicking the *in vivo* airway structure. The ring shape also provides a clear analogue between structure and function of a contractile ASM bundle. As an ASMC-only culture, these constructs still represent a simplified model of the small airway. However, the alignment of ASMCs and abundance

of cell–cell contacts may be advantageous for studying contact-mediated cell signaling. For example, one would expect that in rings containing well-connected bands of ASMCs, there would be opportunities for examining slow-wave depolarizations by way of cell–cell gap junctions. In the absence of cues from other cell types normally found in lung tissue, the rings may also not fully capture the contributions of other cells and structural elements compared to precision cut lung slices or live animal models. Additionally, from a mechanical standpoint, rings that are held open by compressing around the central mandrel are different from what occur in airways *in vivo*, where the tissue is tethered to the surrounding parenchyma, despite similarities in force balance. In addition, the rings are static models that do not undergo changes in stress and strain typical of normal tidal breathing or occasional sighs. The ASMC rings can, however, remain intact and viable for several weeks in culture, allowing long-term observation, which can be useful for characterizing processes that occur over longer timescales, e.g. remodeling of the ECM.

Finally, given the dramatic response of the ASMC rings to TGF-β1, the approach shows promise in assessing the influence of other exogenous factors on ASMC contractile response, and the use of a PDMS device facilities the transition to future design iterations that may seek to include additional co-cultured cell types or anchoring of the ASMC ring about its outer circumference. The integration of the rings with modified lung-on-a-chip systems may allow for future dynamic studies that seek to investigate the influence of cyclic stretch and fluid transport on disease development, representing a bridge or supplement to animal models in the development of novel treatments for small airway disease. Here, the use of a 3D printed device for moulding the PDMS, rather than substrates prepared by traditional photolithographic processing of silicon wafers and resists, may provide opportunity to rapidly prototype new features and designs in an efficient, user-friendly, and cost-effective manner.

Data availability statement

The data that support the findings of this study are available upon reasonable request from the authors.

Acknowledgments

The authors acknowledge the use of the Dalhousie University Cellular & Molecular Digital Imaging Facility. This work was supported by funds from the Canada Research Chairs Program (J P F), the Canada Foundation for Innovation (J P F, Project #33533), the Natural Sciences and Engineering Research Council of Canada (J P F, RGPIN-04298-2016; T A Q, RGPIN-2016-04879; G N M, RGPIN-06929-2017), Canadian Institutes of Health Research (T A Q, MOP 342562), Lung Association of Nova Scotia (J P F and G N M), and Research Nova Scotia (J P F and G N M, MED-EST-2018-1576). J B and J C acknowledge support from the Natural Sciences and Engineering Research Council of Canada Undergraduate Student Research Awards program. The authors acknowledge that Dalhousie University is located in Mi'kma'ki, the ancestral and unceded territory of the Mi'kmaq.

Ethical statement

The D12 airway smooth muscle cell line used throughout this work was originally developed under protocol HREB H2002:150, approved by the Human Research Ethics Board of the University of Manitoba.

ORCID iD

John P Frampton https://orcid.org/0000-0001-6245-1147

References

[1] Fang Y and Eglen R M 2017 Three-dimensional cell cultures in drug discovery and development *SLAS Discov.* **22** 456–72
[2] Langhans S A 2018 Three-dimensional *in vitro* cell culture models in drug discovery and drug repositioning *Front. Pharmacol.* **9** 1–14
[3] Berg I C, Mohagheghian E, Habing K, Wang N and Underhill G H 2021 Microtissue geometry and cell-generated forces drive patterning of liver progenitor cell differentiation in 3D *Adv. Healthcare Mater.* **10** 1–17
[4] Magliaro C, Mattei G, Iacoangeli F, Corti A, Piemonte V and Ahluwalia A 2019 Oxygen consumption characteristics in 3D constructs depend on cell density *Front. Bioeng. Biotechnol.* **7** 251
[5] Riss T and Trask O J 2021 Factors to consider when interrogating 3D culture models with plate readers or automated microscopes *Vitro Cell. Dev. Biol. Animal* **57** 238–56
[6] Boys A J, Barron S L, Tilev D and Owens R M 2020 Building scaffolds for tubular tissue engineering *Front Bioeng. Biotechnol.* **8** 1357
[7] Kamm R D 1999 Airway wall mechanics *Annu. Rev. Biomed. Eng.* **1** 47–72
[8] Hershenson M B, Brown M, Camoretti-Mercado B and Solway J 2008 Airway smooth muscle in asthma *Annu. Rev. Pathol.: Mech. Dis.* **3** 523–55
[9] Dye B R *et al* 2015 *In vitro* generation of human pluripotent stem cell derived lung organoids *Elife* **4** 1–25
[10] Miller A J, Dye B R, Ferrer-Torres D, Hill D R, Overeem A W, Shea L D and Spence J R 2019 Generation of lung organoids from human pluripotent stem cells *in vitro Nat. Protocols* **14** 518–40
[11] Tan Q, Choi K M, Sicard D and Tschumperlin D J 2017 Human airway organoid engineering as a step toward lung regeneration and disease modeling *Biomaterials* **113** 118–32
[12] Hackett T-L *et al* 2009 Induction of epithelial-mesenchymal transition in primary airway epithelial cells from patients with asthma by transforming growth factor-beta1 *Am. J. Respir. Crit. Care Med.* **180** 122–33
[13] Hackett T-L, Singhera G K, Shaheen F, Hayden P, Jackson G R, Hegele R G, Van Eeden S, Bai T R, Dorscheid D R and Knight D A 2011 Intrinsic phenotypic differences of asthmatic epithelium and its inflammatory responses to respiratory syncytial virus and air pollution *Am. J. Respir. Cell Mol. Biol.* **45** 1090–100

[14] Malavia N K, Raub C B, Mahon S B, Brenner M, Panettieri R A and George S C 2009 Airway epithelium stimulates smooth muscle proliferation *Am. J. Respir. Cell Mol. Biol.* **41** 297–304
[15] Huh D 2015 A human breathing lung-on-a-chip *Ann. Am. Thorac. Soc.* **12** S42–4
[16] Benam K H *et al* 2016 Small airway-on-a-chip enables analysis of human lung inflammation and drug responses *in vitro Nat. Methods* **13** 151–7
[17] Huh D, Leslie D C, Matthews B D, Fraser J P, Jurek S, Hamilton G A, Thorneloe K S, McAlexander M A and Ingber D E 2012 A human disease model of drug toxicity-induced pulmonary edema in a lung-on-a-chip microdevice *Sci. Transl. Med.* **4** 159ra147
[18] Humayun M, Chow C W and Young E W K 2018 Microfluidic lung airway-on-a-chip with arrayable suspended gels for studying epithelial and smooth muscle cell interactions *Lab Chip* **18** 1298–309
[19] Nesmith A P, Agarwal A, McCain M L and Parker K K 2014 Human airway musculature on a chip: an *in vitro* model of allergic asthmatic bronchoconstriction and bronchodilation *Lab Chip* **14** 3925–36
[20] Legant W R, Pathak A, Yang M T, Deshpande V S, McMeeking R M and Chen C S 2009 Microfabricated tissue gauges to measure and manipulate forces from 3D microtissues *Proc. Natl Acad. Sci. USA* **106** 10097–102
[21] West A R *et al* 2013 Development and characterization of a 3D multicell microtissue culture model of airway smooth muscle *Am. J. Physiol. Lung Cell Mol. Physiol.* **304** 4–16
[22] Walker M, Rizzuto P, Godin M and Pelling A E 2020 Structural and mechanical remodeling of the cytoskeleton maintains tensional homeostasis in 3D microtissues under acute dynamic stretch *Sci. Rep.* **10** 1–16
[23] Chen Z, Wang Q, Asmani M, Li Y, Liu C, Li C, Lippmann J M, Wu Y and Zhao R 2016 Lung microtissue array to screen the fibrogenic potential of carbon nanotubes *Sci. Rep.* **6** 1–11
[24] Grigoryan B *et al* 2019 Multivascular networks and functional intravascular topologies within biocompatible hydrogels *Science* **364** 458–64
[25] Park J Y, Ryu H, Lee B, Ha D H, Ahn M, Kim S, Kim J Y, Jeon N L and Cho D W 2019 Development of a functional airway-on-a-chip by 3D cell printing *Biofabrication* **11** 015002
[26] Barreiro Carpio M, Dabaghi M, Ungureanu J, Kolb M R, Hirota J A and Moran-Mirabal J M 2021 3D Bioprinting strategies, challenges, and opportunities to model the lung tissue microenvironment and its function *Front. Bioeng. Biotechnol.* **9** 1–24
[27] Dickman C T D, Russo V, Thain K, Pan S, Beyer S T, Walus K, Getsios S, Mohamed T and Wadsworth S J 2020 Functional characterization of 3D contractile smooth muscle tissues generated using a unique microfluidic 3D bioprinting technology *FASEB J.* **34** 1652–64
[28] An S S *et al* 2009 Cell stiffness, contractile stress and the role of extracellular matrix *Biochem. Biophys. Res. Commun.* **382** 697–703
[29] Tseng H, Gage J A, Raphael R M, Moore R H, Killian T C, Grande-Allen K J and Souza G R 2013 Assembly of a three-dimensional multitype bronchiole coculture model using magnetic levitation *Tissue Eng.* C **19** 665–75
[30] Fairbank N J, Connolly S C, Mackinnon J D, Wehry K, Deng L and Maksym G N 2008 Airway smooth muscle cell tone amplifies contractile function in the presence of chronic cyclic strain *Am. J. Physiol. Lung Cell Mol. Physiol.* **295** L479–88
[31] Ijpma G, Panariti A, Lauzon A M and Martin J G 2017 Directional preference of airway smooth muscle mass increase in human asthmatic airways *Am. J. Physiol. Lung Cell Mol. Physiol.* **312** L845–54
[32] Dean D M, Napolitano A P, Youssef J and Morgan J R 2007 Rods, tori, and honeycombs: the directed self-assembly of microtissues with prescribed microscale geometries *FASEB J.* **21** 4005–12
[33] Strobel H A, Dikina A D, Levi K, Solorio L D, Alsberg E and Rolle M W 2017 Cellular self-assembly with microsphere incorporation for growth factor delivery within engineered vascular tissue rings *Tissue Eng.* A **23** 143–55
[34] Strobel H A, Calamari E L, Alphonse B, Hookway T A and Rolle M W 2018 Fabrication of custom agarose wells for cell seeding and tissue ring self-assembly using 3D-printed molds *J. Vis. Exp.* e56618
[35] Adebayo O, Hookway T A, Hu J Z, Billiar K L and Rolle M W 2013 Self-assembled smooth muscle cell tissue rings exhibit greater tensile strength than cell-seeded fibrin or collagen gel rings *J. Biomed. Mater. Res.* A **101** 428–37
[36] Xie S, Sukkar M B, Issa R, Khorasani N M and Chung K F 2007 Mechanisms of induction of airway smooth muscle hyperplasia by transforming growth factor-beta *Am. J. Physiol. Lung Cell Mol. Physiol.* **293** L245–53
[37] Woodman L, Siddiqui S, Cruse G, Sutcliffe A, Saunders R, Kaur D, Bradding P and Brightling C 2008 Mast cells promote airway smooth muscle cell differentiation via autocrine up-regulation of TGF- 1 *J. Immunol.* **181** 5001–7
[38] Redington A E, Madden J, Frew A J, Djukanovic R, Roche W R, Holgate S T and Howarth P H 1997 Transforming growth factor- β1 in asthma measurement in bronchoalveolar lavage Fluid *Am. J. Respir. Crit. Care Med.* **156** 642–7
[39] Tjong J, Teixeira A G and Frampton J P 2020 Solvent extraction of 3D printed molds for soft lithography *Lab Chip* (available at: https://blogs.rsc.org/chipsandtips/2020/06/12/solvent-extraction-of-3d-printed-molds-for-soft-lithography/?doing_wp_cron=1677162816.1219120025634765625000)
[40] Wang J C, Liu W, Tu Q, Ma C, Zhao L, Wang Y, Ouyang J, Pang L and Wang J 2015 High throughput and multiplex localization of proteins and cells for *in situ* micropatterning using pneumatic microfluidics *Analyst* **140** 827–36
[41] Gosens R, Stelmack G L, Dueck G, McNeill K D, Yamasaki A, Gerthoffer W T, Unruh H, Gounni A S, Zaagsma J and Halayko A J 2006 Role of caveolin-1 in p42/p44 MAP kinase activation and proliferation of human airway smooth muscle *Am. J. Physiol. Lung Cell Mol. Physiol.* **291** L523–34
[42] MacDonald E A, Madl J, Greiner J, Ramadan A F, Wells S M, Torrente A G, Kohl P, Rog-Zielinska E A and Quinn T A 2020 Sinoatrial node structure, mechanics, electrophysiology and the chronotropic response to stretch in rabbit and mouse *Front. Physiol.* **11** 809
[43] Vandesompele J, De Preter K, Pattyn F, Poppe B, Van Roy N, De Paepe A and Speleman F 2002 Accurate normalization of real-time quantitative RT-PCR data by geometric averaging of multiple internal control genes *Genome Biol.* **3** 1–12
[44] Tan Y, Richards D J, Trusk T C, Visconti R P, Yost M J, Kindy M S, Drake C J, Argraves W S, Markwald R R and Mei Y 2014 3D printing facilitated scaffold-free tissue unit fabrication *Biofabrication* **6** 024111
[45] Correia C *et al* 2018 3D aggregate culture improves metabolic maturation of human pluripotent stem cell derived cardiomyocytes *Biotechnol. Bioeng.* **115** 630–44
[46] Gwyther T A, Hu J Z, Christakis A G, Skorinko J K, Shaw S M, Billiar K L and Rolle M W 2011 Engineered vascular tissue fabricated from aggregated smooth muscle cells *Cells Tissues Organs (Print)* **194** 13–24
[47] Dash B C *et al* 2016 Tissue-engineered vascular rings from human iPSC-derived smooth muscle cells *Stem Cell Rep.* **7** 19–28
[48] Napolitano A P, Chai P, Dean D M and Morgan J R 2007 Dynamics of the self-assembly of complex cellular aggregates on micromolded nonadhesive hydrogels *Tissue Eng.* **13** 2087–94
[49] Wakatsuki T, Kolodney M S, Zahalak G I and Elson E L 2000 Cell mechanics studied by a reconstituted model tissue *Biophys. J* **79** 2353–68

[50] Lin R Z and Chang H Y 2008 Recent advances in three-dimensional multicellular spheroid culture for biomedical research *Biotechnol. J.* **3** 1172–84
[51] Alvarez-Pérez J, Ballesteros P and Cerdán S 2005 Microscopic images of intraspheroidal pH by 1H magnetic resonance chemical shift imaging of pH sensitive indicators *Magn. Reson. Mater. Phys. Biol. Med.* **18** 293–301
[52] Halayko A J and Solway J 2001 Molecular mechanisms of phenotypic plasticity in smooth muscle cells *J. Appl. Physiol.* **90** 358–68
[53] Halayko A J, Camoretti-Mercado B, Forsythe S M, Vieira J E, Mitchell R W, Wylam M E, Hershenson M B and Solway J 1999 Divergent differentiation paths in airway smooth muscle culture: induction of functionally contractile myocytes *Am. J. Physiol.* **276** 197–206
[54] Codd S L, Lambert R K, Alley M R and Pack R J 1994 Tensile stiffness of ovine tracheal wall *J. Appl. Physiol.* **76** 2627–35
[55] Eskandari M, Arvayo A L and Levenston M E 2018 Mechanical properties of the airway tree: heterogeneous and anisotropic pseudoelastic and viscoelastic tissue responses *J. Appl. Physiol.* **125** 878–88
[56] Ebina M, Takahashi T, Chiba T and Motomiya M 1993 Cellular hypertrophy and hyperplasia of airway smooth muscles underlying bronchial asthma: a 3D morphometric study *Am. Rev. Respir. Dis.* **148** 720–6
[57] James A L, Elliot J G, Jones R L, Carroll M L, Mauad T, Bai T R, Abramson M J, McKay K O and Green F H 2012 Airway smooth muscle hypertrophy and hyperplasia in asthma *Am. J. Respir. Crit. Care Med.* **185** 1058–64
[58] Lambert R K, Wiggs B R, Kuwano K, Hogg J C and D P P 1993 Functional significance of increased airway smooth muscle in asthma and COPD *J. Appl. Physiol.* **74** 2771–81
[59] Oliver M N, Fabry B, Marinkovic A, Mijailovich S M, Butler J P and Fredberg J J 2007 Airway hyperresponsiveness, remodeling, and smooth muscle mass: right answer, wrong reason? *Am. J. Respir. Cell Mol. Biol.* **37** 264–72
[60] Bossé Y and Rola-Pleszczynski M 2007 Controversy surrounding the increased expression of TGF beta 1 in asthma *Respir. Res.* **8** 66
[61] Duvernelle C, Freund V and Frossard N 2003 Transforming growth factor-beta and its role in asthma *Pulm. Pharmacol. Ther.* **16** 181–96
[62] Ojiaku C A, Yoo E J and Panettieri R A 2017 Transforming growth factor β1 function in airway remodeling and hyperresponsiveness. The missing link? *Am. J. Respir. Cell Mol. Biol.* **56** 432–42
[63] Halwani R, Al-Muhsen S, Al-Jahdali H and Hamid Q 2011 Role of transforming growth factor-β in airway remodeling in asthma *Am. J. Respir. Cell Mol. Biol.* **44** 127–33
[64] Bossé Y, Stankova J and Rola-Pleszczynski M 2010 Transforming growth factor-beta1 in asthmatic airway smooth muscle enlargement: is fibroblast growth factor-2 required? Clin *Exp. Allergy* **40** 710–24
[65] Schuliga M, Javeed A, Harris T, Xia Y, Qin C, Wang Z, Zhang X, Lee P V S, Camoretti-Mercado B and Stewart A G 2013 Transforming growth factor-β-induced differentiation of airway smooth muscle cells is inhibited by fibroblast growth factor-2 *Am. J. Respir. Cell Mol. Biol.* **48** 346–53
[66] Fukushima T *et al* 2017 γ-Tocotrienol inhibits TGF-β1-induced contractile phenotype expression of human airway smooth muscle cells *Yonago Acta Med.* **60** 16–23
[67] Rattan S and Ali M 2015 Role of SM22 in the differential regulation of phasic vs. tonic smooth muscle Am *Am. J. Physiol.—Gastrointest. Liver Physiol.* **308** G605–12
[68] Makinde T, Murphy R F and Agrawal D K 2007 The regulatory role of TGF-beta in airway remodeling in asthma *Immunol. Cell Biol.* **85** 348–56
[69] Goldsmith A M, Bentley J K, Zhou L, Jia Y, Bitar K N, Fingar D C and Hershenson M B 2006 Transforming growth factor-beta induces airway smooth muscle hypertrophy *Am. J. Respir. Cell Mol. Biol.* **34** 247–54
[70] Slats A M *et al* 2008 Expression of smooth muscle and extracellular matrix proteins in relation to airway function in asthma J *Allergy Clin. Immunol.* **121** 1196–202
[71] Annoni R *et al* 2012 Extracellular matrix composition in COPD *Eur. Respir. J.* **40** 1362–73
[72] Yu L, Hébert M C and Zhang Y E 2002 TGF-β receptor-activated p38 MAP kinase mediates Smad-independent TGF-β responses *EMBO J.* **21** 3749–59
[73] Smith P G, Roy C, Zhang Y N and Chauduri S 2003 Mechanical stress increases RhoA activation in airway smooth muscle cells *Am. J. Respir. Cell Mol. Biol.* **28** 436–42
[74] Ojiaku C A, Cao G, Zhu W, Yoo E J, Shumyatcher M, Himes B E, An S S and Panettieri R A 2018 TGF-β1 evokes human airway smooth muscle cell shortening and hyperresponsiveness via Smad3 *Am. J. Respir. Cell Mol. Biol.* **58** 575–84
[75] Ojiaku C A *et al* 2019 Transforming growth factor-β1 decreases β2-agonist–induced relaxation in human airway smooth muscle *Pharm. Fac. Artic. Res.* **61** 209–18